Simultaneously Counting and Extracting Endmembers in a Hyperspectral Image Based on Divergent Subsets

Xuanwen Tao, *Student Member, IEEE*, Tingwei Cui, Antonio Plaza, *Fellow, IEEE*, and Peng Ren, *Senior Member, IEEE*

Abstract—Most existing endmember extraction techniques require prior knowledge about the number of endmembers in a hyperspectral image. The number of endmembers is normally estimated by a separate procedure, whose accuracy has a large influence on the endmember extraction performance. In order to bridge the two seemingly independent but, in fact, highly correlated procedures, we develop a new endmember estimation strategy that simultaneously counts and extracts endmembers. We consider a hyperspectral image as a hyperspectral pixel set and define the subset of pixels that are most different from one another as the divergent subset (DS) of the hyperspectral pixel set. The DS is characterized by the condition that any additional pixel would increase the likeness within the DS and, thus, reduce its divergent degree. We use the DS as the endmember set, with the number of endmembers being the subset cardinality. To render a practical computation scheme for identifying the DS, we reformulate it in terms of a quadratic optimization problem with a numerical solution. In addition to operating as an endmember estimation algorithm by itself, the DS method can also co-operate with existing endmember extraction techniques by transforming them into a novel and more effective schemes. Experimental results validate the effectiveness of the DS methodology in simultaneously counting and extracting endmembers not only as an individual algorithm but also as a foundation algorithm for improving existing methods. Our full code is released for public evaluation.[1]

Index Terms—Divergent subset (DS), endmember estimation, hyperspectral image, spectral unmixing.

Xuanwen Tao and Peng Ren are with the College of Oceanography and Space Informatics, China University of Petroleum (East China), Qingdao 266580, China (e-mail: txw_upc@126.com; pengren@upc.edu.cn).

Tingwei Cui is with the School of Atmospheric Sciences, Sun Yat-sen University, Zhuhai 519000, China, also with the Guangdong Province Key Laboratory for Climate Change and Natural Disaster Studies, Sun Yat-sen University, Zhuhai 519000, China, and also with the Southern Marine Science and Engineering Guangdong Laboratory (Zhuhai), Sun Yat-sen University, Zhuhai 519000, China (e-mail: cuitw@mail.sysu.edu.cn).

Antonio Plaza is with the Hyperspectral Computing Laboratory, Department of Technology of Computers and Communications, University of Extremadura, E-10071 Caceres, Spain (e-mail: aplaza@unex.es).

Color versions of one or more of the figures in this article are available online at https://ieeexplore.ieee.org.

Digital Object Identifier 10.1109/TGRS.2020.2992542

[1]https://github.com/xuanwentao/DivergentSubset

I. Introduction

REMOTELY sensed hyperspectral images [1] provide detailed information about different materials on the surface of the earth. The detailed spectral information provided by these images has been widely utilized for object classification [2]–[4], target identification [5]–[7], change detection [8]–[10], and so on. One common problem associated with hyperspectral images is low spatial resolution, which inevitably leads to mixed pixels. A mixed pixel in a hyperspectral image covers several types of materials, and the corresponding spectrum is a mixture of several ground cover spectra known as endmembers. The mixed pixel phenomenon complicates the process of classifying one hyperspectral pixel into one unique material type. To address the ambiguity, spectral unmixing techniques [11]–[13] have been comprehensively investigated for the purpose of extracting endmembers. These techniques decompose each mixed pixel into a proportional composition of endmembers. The constituent proportion with respect to different types of materials [14] for each pixel is referred to as the abundance.

One fundamental requirement for effectively performing spectral unmixing is to accurately identify the endmembers of a hyperspectral image. This is normally achieved by two steps. First, the number of endmembers, i.e., the number of types of pure pixels (possibly with noise) in the image, is determined. Second, according to the number, the endmembers are extracted from the hyperspectral image. We refer to the overall procedures regarding estimating the number of endmembers and endmember extraction as endmember estimation [15] in this article. In Section I-A, we review the literature about estimating the number of endmembers and endmember extraction. In Section I-B, we briefly describe the major contributions of this article in terms of presenting a new endmember estimation framework that simultaneously determines the number of endmembers and extracts their spectral signatures.

A. Literature Review

Determining the number of endmembers [16], [17] is the first step of endmember estimation. In the literature, the number of endmembers is normally regarded as prior knowledge. However, such prior knowledge is almost unavailable in an arbitrary hyperspectral image. In this scenario, if the number

of endmembers is not accurately determined, most existing endmember extraction techniques cannot operate properly. The limitation regarding an unknown number of endmembers hinders most existing endmember extraction techniques from an operational viewpoint. To address the limitation, various algorithms have been developed for estimating the number of endmembers. Particularly, information theory-based algorithms, eigenvalue thresholding algorithms, and geometry characterization methods are three main families of techniques for estimating the number of endmembers. The first family includes information-theoretic criteria based on minimum description length [18], Akaike's information criterion [19], the Bayesian information criterion [20], and so on. Different models have been developed for encoding a negative data log-likelihood term, based on which an accurate estimation of the number of endmembers is expected to be obtained when the model achieves a global optimum. These strategies depend on the empirical configuration of specific mixed models or likelihood functions, and inappropriate configurations would cause estimation errors of the number of endmembers. The second family is related to the eigenvalue thresholding schemes [21]–[23]. A threshold is applied to eigendecomposition results from subspace analysis, such as principal component analysis (PCA) [24], hyperspectral signal subspace by minimum error (Hysime) [25], and the so-called Harsanyi–Farrand–Chang (HFC) analysis [26]. The PCA-based approaches aim to characterize a cutoff gap between the eigenvalues caused by signals and noise. However, the variation between the two eigenvalues may be insignificant, possibly resulting in an incorrect estimation of the number of endmembers. The Hysime approach conducts spectrum noise and the noise covariance estimation, which requires high computational complexity. The HFC approach requires a constant false alarm rate, which has an influence on the estimated number of endmembers. The third family is characterized by the geometry-based estimation of the number of endmembers (GENE), which includes the convex hull (GENE-CH) algorithm, the affine hull (GENE-AH) algorithm [27], and so on. They assume that data samples should lie within a convex hull (CH) or an affine hull (AH) with the endmember signatures as vertices. GENE algorithms operate along with an endmember extraction algorithm (EEA). In this scenario, a maximum hull volume would stop the EEA from extracting the next endmember signature. Therefore, the GENE algorithms depend on the effectiveness of the EEA used, and different EEAs cause different accuracies for counting endmembers.

Once the number of endmembers has been determined, the subsequent processing step for endmember estimation is to extract the determined number of endmember signatures [28]. The N-FINDR algorithm and its derivatives, such as cofactor NFINDR [29], geometric distance constrained N-FINDR [30], and locality preserving N-FINDR [31], are representative methods for endmember extraction. The N-FINDR-based algorithms are devised to search for a simplex with the greatest volume. The pixels that form the simplex are endmembers. The N-FINDR algorithms repeatedly extract endmembers, and the initial endmember matrix chosen from all pixel combinations is random. The simplex growing algorithm (SGA) [32] seeks an endmember convex geometry with the minimum volume, and it also requires specific initialization. To avoid repeated identification of an endmember, the automatic target generation process (ATGP) [33] is proposed to extract endmembers by utilizing the notion of orthogonal subspace projection. The alternating decoupled volume max–min (ADVMM) [34] and successive decoupled volume max–min (SDVMM) [34] are developed for addressing the worst case simplex volume maximization problem by alternating optimization and by successive optimization, respectively. Specially, alternating volume maximization (AVMAX) [35] and successive volume maximization (SVMAX) [35] have been exploited to characterize more comprehensive criteria. Negative abundance-oriented (NABO) [36] uses the pixels outside the hull as alternative candidate endmembers. Standard least-square optimization is exploited to achieve estimates of endmember combinations following the geometrical properties of hyperspectral signatures [37]. The improved quantum-behaved particle swarm optimization (IQPSO) [38] is a novel optimization algorithm for hyperspectral endmember extraction. It is the first solid work to construct quantum mechanics-driven evolutionary computing algorithms, surpassing state-of-the-art evolutionary computing EEA. In this scenario, the accurate number of endmembers is necessary for effective endmember extraction [39].

B. Contributions

As reviewed in Section I-A, existing studies for estimating the number of endmembers and for extracting endmembers are performed as two independent topics in the literature. Most EEAs assume the known number of endmembers, but the estimation algorithms of the number of endmembers tend to be characterized by independent methods that may not seamlessly benefit the EEAs. One overall goal of this article is to bridge these two seemingly independent but, in fact, highly related procedures in terms of establishing a unifying endmember estimation framework. The major contributions of this article are threefold.

1) We develop an overall endmember estimation framework that simultaneously determines the number of endmembers and extracts their endmember signatures. Specifically, we define a new concept, i.e., the divergent subset (DS), the computation of which extracts endmembers without prior knowledge of the number of endmembers. In addition, the cardinality of the DS is naturally in accordance with the number of endmembers. Our DS method is highly motivated by the concept of the dominant set [40]–[42], which aims at extracting a homogeneous cluster from a set. However, a DS and a dominant set are defined in opposite ways. Specifically, the DS seeks the largest difference, but the dominant set characterizes the greatest homogeneity. Be that as it may, the motivations and computational techniques concerning the dominant set provide a tractable vehicle for modeling our DS. To the best of our knowledge, we are among the first to develop an automatic framework that simultaneously counts and extracts endmembers.

2) The DS framework provides a strategy for transforming existing endmember extraction methods into a novel and more accurate ones that do not require the knowledge of the number of endmembers. To this end, the DS co-operates with one arbitrary existing endmember extraction method. As reviewed in Section I-A, endmember extraction normally requires the knowledge of the number of endmembers. We artificially set the number of endmembers to be a value that is reasonably larger than the actual number of endmembers and, subsequently, perform the endmember extraction. In this scenario, the real endmembers are a subset of the extracted pixels, which are redundant and with less discriminativeness. We then apply the DS computation to the extracted pixel set. The DS finely prunes the coarsely extracted pixels, resulting in accurate endmembers with their number automatically determined. Therefore, the DS framework not only is capable of simultaneously counting and extracting endmembers by itself but also can be considered as a foundation stone for developing novel endmember extraction schemes based on arbitrary existing endmember extraction methods. The resulting endmember extraction schemes have no requirement of knowing the number of endmembers but exhibit the potential to provide better accuracy than the original endmember extraction method.

3) The DS has the property that it encompasses pixels with the largest unlikeness and any additional pixel would decrease its unlikeness. Such property renders the DS robust in both endmember counting and endmember extraction. Experiments validate the advantages of the DS over state-of-the-art endmember counting methods and endmember extraction methods.

C. Paper Outline

The rest of this article is organized as follows. In Section II, we present a series of definitions and then give a recursive definition of a DS. In Section III, we explain the possibility of using a DS to characterize endmembers. In Section IV, we introduce a closed-form formulation of a DS. In Section V, we describe how to numerically compute the DS. In Section VI, we describe how to employ the DS to transform existing endmember extraction methods into new effective schemes. In Section VII, we empirically evaluate the performance of the DS method in extracting and counting endmembers on both synthetic and real data. In Section VIII, we conclude this article with some remarks and hints at plausible future research lines.

II. RECURSIVE DEFINITION OF A DS

We consider a hyperspectral image with L-band and N pixels as a hyperspectral pixel set $\mathbf{X} = [\mathbf{x}_1, \mathbf{x}_2, \ldots, \mathbf{x}_n, \ldots, \mathbf{x}_N] \in \mathbb{R}^{L \times N}$, in which the nth pixel $\mathbf{x}_n = [x_{1n}, x_{2n}, \ldots, x_{Ln}]^T \in \mathbb{R}^{L \times 1}$ is an L-dimensional vector representing its L-band spectrum. Let $\mathbf{D} \in \mathbb{R}^{N \times N}$ denote the feature distance matrix, and the (i, j)th element d_{ij} of $\mathbf{D}$ represents the feature distance

between the ith and jth hyperspectral pixels in a feature space. The feature distance d_{ij} is computed by the Euclidean distance

$$
d_{ij} = \| \mathbf{x}_i - \mathbf{x}_j \|_2 \\
= \sqrt{(x_{1i} - x_{1j})^2 + \cdots + (x_{Li} - x_{Lj})^2}. \tag{1}
$$

Let $V = \{1, 2, \ldots, N\}$ denote the index set for all pixels in the hyperspectral image. We give the following definitions regarding a subset $E \in V$ and derive the most important concept in our work, i.e., the DS, at the end of this section.

Definition 1: We define the intrafeature distance $\overline{d}_E(j)$ for a pixel $j \in E$ with respect to the subset E as follows:

$$
\overline{d}_E(j) = \frac{1}{|E|} \sum_{i \in E} d_{ij}. \tag{2}
$$

It is easy to observe from (2) that $\overline{d}_{\{j\}}(j) = 0$ because $d_{jj} = 0$ represents a self-feature distance of the pixel j. The intrafeature distance $\overline{d}_E(j)$ measures the average feature distance between the pixel $j \in E$ and the rest of pixels in E. It also reflects how different the pixel $j \in E$ is from the rest of pixels in E. A large value of the intrafeature distance $\overline{d}_E(j)$ implies that the pixel $j \in E$ is generally very different from the rest of pixels in E.

Definition 2: For the pixels $j \in E$ and $i \notin E$, we define the incremental feature distance $\Delta d_E^j(i)$ of the feature distance d_{ij} over the intrafeature distance $\overline{d}_E(j)$ as follows:

$$
\Delta d_E^j(i) = d_{ij} - \overline{d}_E(j). \tag{3}
$$

The incremental feature distance $\Delta d_E^j(i)$ reflects a relative feature distance between the pixel $i \notin E$ and the pixel set E, with the pixel $j \in E$ being an intermediary between them. It can be either positive or negative. A positive value of $\Delta d_E^j(i)$ implies that the feature distance between the pixel $i \notin E$ and the pixel $j \in E$ is greater than the average feature distance between the pixel $j \in E$ and those in E. In other words, the difference between the pixels i and j is greater than the general difference between the pixel j and those in E. A negative value of $\Delta d_E^j(i)$ implies that the feature distance between the pixel $i \notin E$ and the pixel $j \in E$ is shorter than the average feature distance between the pixel $j \in E$ and those in E. That is, the difference between the pixels i and j is less than the general difference between the pixel j and those in E.

Definition 3: We define the divergent grade $d_E(i)$ of the pixel $i \in E$ with respect to the subset E as follows:

$$
d_E(i) = \begin{cases} 1, & \text{if } |E| = 1 \\ \sum_{j \in E \setminus i} \Delta d_{E \setminus i}^j(i) d_{E \setminus i}(j), & \text{otherwise.} \end{cases} \tag{4}
$$

The divergent grade measures, in the feature space, how distant one pixel is from all the pixels in the set. It can be either positive or negative. A positive value of the divergent grade $d_E(i)$ reflects that the pixel i is quite different from most pixels in E. On the other hand, a negative value of the divergent grade $d_E(i)$ indicates the indiscriminate resemblance of the pixel i to the subset E.

Definition 4: We define the divergent degree of the pixel subset E as follows:

$$
\mathcal{D}(E) = \sum_{i \in E} d_E(i). \tag{5}
$$

The divergent degree measures, in the feature space, how far apart each pixel in E is from one another. It reflects the unlikeness within a set. A big divergent degree value reflects that any pair of pixels in E is very distant in the feature space, i.e., they are quite different. On the other hand, a small divergent degree implies that in E, some of the pixels are not so far apart from another, such that they tend to be close to one another in the feature space, i.e., at least some of the pixels are very similar.

Proposition 1: For a nonempty set V in which the pixel feature distances are not unique, there exists a subset $\hat{E} \subseteq V$ that satisfies the following two conditions.

1) $\forall j \in \hat{E},\ d_{\hat{E}}(j) > 0$.
2) $\forall i \notin \hat{E},\ d_{\hat{E} \bigcup i}(i) < 0$.

Proof: The proof of the proposition requires a Lagrangian formulation. The evidence for the proposition can then be identified via the Karush–Kuhn–Tucker (KKT) conditions. The details can be found within the proof of Proposition 2 in Section IV.

Definition 5: For a set V, we define the subset which satisfies the two conditions in Proposition 2 as the DS $\hat{E}$ of the set V. Equivalently, a DS is the one that has the largest divergent degree.

The two conditions in Proposition 2 describe the two main properties of a DS $\hat{E}$. The first condition favors the internal unlikeness of pixels within $\hat{E}$. It requires that each pixel should be far apart from any other pixels within $\hat{E}$. The second condition excludes external likeness. The incorporation of an additional pixel outside $\hat{E}$ into $\hat{E}$ would increase its likeness in terms of introducing a negative divergent grade. Therefore, the additional pixel would decrease the divergence degree and should be excluded, and we use the DS $\hat{E}$ as the endmember set, and its number is the number of endmembers.

III. DS OF PIXELS AS ENDMEMBERS

The goal of endmember extraction from a hyperspectral image is to identify a subset of pixels that are most different from one another. The divergent degree provides a meaningful tool for measuring the unlikeness of pixels within a subset, with respect to pixels outside the subset. By Definition 5, a DS represents a group of pixels with the largest divergent degree. We, thus, consider the DS $\hat{E}$ as the endmembers of the hyperspectral image. Furthermore, once a DS is determined, the number of endmembers can be accordingly determined in terms of its cardinality.

However, it is almost intractable to compute a DS based on Proposition 2 and Definition 5. Specifically, according to (4), recursively computing the divergent grade $d_E(i)$ of the pixel $i \in E$ with respect to the subset E is computationally exhaustive. To render a practical computation scheme, we introduce a closed-form formulation of the DS in Section IV.

IV. CLOSED-FORM FORMULATION OF THE DS

We reformulate the concept of DS in terms of Lemma 2 and Proposition 2 in this section.

Lemma 1: The divergent grade $d_{\hat{E} \bigcup i}(i)$ can be computed as follows:

$$d_{\hat{E} \bigcup i}(i) = \sum_{k \in \hat{E}} (d_{ik} - d_{jk}) d_{\hat{E}}(k). \tag{6}$$

Proof: The computing method for $d_{\hat{E} \bigcup i}(i)$ requires elementary properties of the determinant. The detailed proof can be found in [41, p. 98].

Proposition 2: The DS can be computed in terms of solving the following quadratic optimization problem:

$$\hat{\mathbf{y}} = \arg\max_{\mathbf{y}} \frac{1}{2} \mathbf{y}^{\mathrm{T}} \mathbf{D} \mathbf{y}$$

$$\text{s. t.}\quad y_i \geq 0,\quad \sum_{i=1}^{N} y_i = 1. \tag{7}$$

The nonzero elements in the optimal $\hat{\mathbf{y}} \in \mathbb{R}^{N \times 1}$ indicate the DS.

Proof: We commence by the following setting:

$$\hat{y}_k = \begin{cases} \dfrac{d_{\hat{E}}(k)}{\mathcal{D}(\hat{E})}, & \text{if } k \in \hat{E} \\ 0, & \text{otherwise.} \end{cases} \tag{8}$$

According to Definition 5, we have $\mathcal{D}(\hat{E}) = \sum_{k \in \hat{E}} d_{\hat{E}}(k)$. According to condition 1 of Proposition 2, for $k \in \hat{E}$, $d_{\hat{E}}(k) > 0$. Therefore, the setting (8) plays the same role with the conditions $y_i \geq 0$ and $\sum_{i=1}^{N} y_i = 1$ in the optimization problem (7). It follows condition 1 of Proposition 2.

According to the second condition of Proposition 2, for $i \notin \hat{E}$, $d_{\hat{E} \bigcup i}(i) < 0$. Therefore, we have

$$\frac{d_{\hat{E} \bigcup i}(i)}{\mathcal{D}(\hat{E})} < 0. \tag{9}$$

According to Lemma 1 and the setting (8), we have

$$\begin{aligned} \frac{d_{\hat{E} \bigcup i}(i)}{\mathcal{D}(\hat{E})} &= \frac{\sum_{k \in \hat{E}} (d_{ik} - d_{jk}) d_{\hat{E}}(k)}{\mathcal{D}(\hat{E})} \\ &= \sum_{k \in \hat{E}} \left(d_{ik} \frac{d_{\hat{E}}(k)}{\mathcal{D}(\hat{E})} + d_{jk} \frac{d_{\hat{E}(k)}}{\mathcal{D}(\hat{E})} \right) \\ &= \sum_{k \in \hat{E}} d_{ik} \hat{y}_k - \sum_{k \in \hat{E}} d_{jk} \hat{y}_k \\ &= (\mathbf{D}\hat{\mathbf{y}})_i - (\mathbf{D}\hat{\mathbf{y}})_j \end{aligned} \tag{10}$$

where $(\mathbf{D}\hat{\mathbf{y}})_i$ and $(\mathbf{D}\hat{\mathbf{y}})_j$ represent the ith and jth elements of $\mathbf{D}\hat{\mathbf{y}}$, respectively.

Based on (9) and (10), we have the relation between one pixel $i \notin \hat{E}$ and one pixel $j \in \hat{E}$ formulated by using $\mathbf{D}$ and $\hat{\mathbf{y}}$ as follows:

$$(\mathbf{D}\hat{\mathbf{y}})_i - (\mathbf{D}\hat{\mathbf{y}})_j < 0. \tag{11}$$

The relation in (11) follows condition 2 of Proposition 2. Therefore, the relations in (8) and (11) satisfy the two conditions of Proposition 2, and they conceptually characterize a DS. We then investigate whether the optimization problem (7) leads to the same relations as (8) and (11).

As discussed earlier, the conditions $y_i \geq 0$ and $\sum_{i=1}^{N} y_i = 1$ for the optimization problem (7) are in accordance with the

setting (8). Therefore, they follow condition 1 of Proposition 2. Furthermore, the Lagrangian function for the optimization problem (7) is given as

$$L(\hat{\mathbf{y}}, \lambda, \gamma) = -\frac{1}{2}\hat{\mathbf{y}}^T \mathbf{D}\hat{\mathbf{y}} + \lambda(\sum_{k \in \hat{E}} \hat{y}_k - 1) - \sum_{k \in \hat{E}} \gamma_k \hat{y}_k. \quad (12)$$

The KKT conditions for the optimization problem in (7) require

$$\frac{\partial L}{\partial \hat{y}_k} = -(\mathbf{D}\hat{\mathbf{y}})_k + \lambda - \gamma_k = 0$$
$$\hat{y}_k \gamma_k = 0$$
$$\gamma_k \geq 0. \quad (13)$$

Based on (13), we have

$$(\mathbf{D}\hat{\mathbf{y}})_k = \lambda - \gamma_k. \quad (14)$$

In addition, the complementary slackness of the KKT conditions has specific requirements for the term $\hat{y}_k \gamma_k = 0$ as follows:

$$\forall k \text{ at } \hat{y}_k = 0, \quad \text{it is required that } \gamma_k > 0$$
$$\forall k \text{ at } \hat{y}_k > 0, \quad \text{it is required that } \gamma_k = 0.$$

The proposition claims that one nonzero $\hat{y}_k > 0$ indicates an endmember. According to the complementary slackness, we have

$$\gamma_i > 0 \quad \text{for } i \notin \hat{E}$$
$$\gamma_j = 0 \quad \text{for } j \in \hat{E}. \quad (15)$$

Based on (14) and (15), we have

$$(\mathbf{D}\hat{\mathbf{y}})_i - (\mathbf{D}\hat{\mathbf{y}})_j = (\lambda - \gamma_i) - (\lambda - \gamma_j)$$
$$= -\gamma_i$$
$$< 0. \quad (16)$$

We observe that the relation in (16), which is derived from the closed-form (7), is consistent with the relation in (11), which follows condition 2 of Proposition 2. This proves that the closed-form (7) and Definition 5 provide equivalent formulations for characterizing a DS. This completes the proof.

The relation in (16) is obtained subject to the KKT conditions that are the necessary conditions of the closed-form formulation (7) of a DS. The necessity proves the existence of a DS, which is claimed in Proposition 2.

It is worth noting that the solution y_i of the optimization problem (7) not only extracts the endmember signatures in terms of its nonzero elements but also indicates the number of endmembers by counting the nonzero elements. The number of nonzero elements in $\mathbf{y}$ is the cardinality of the DS and is equal to the number of endmembers. Therefore, our DS method simultaneously extracts endmember signatures and determines their number.

Though Proposition 2 provides a principled manner for formulating a DS, it is still difficult for us to obtain an analytical solution. We will describe how to numerically compute the optimization problem (7) in Section V.

V. NUMERICAL COMPUTATION OF THE DS

We follow the strategy of replicator dynamics in evolutionary game theory [43] to numerically compute the solution for the optimization problem (7) as follows:

$$y_i^{\text{new}} = y_i \frac{(\mathbf{D})_i^T \mathbf{y}}{\mathbf{y}^T \mathbf{D}\mathbf{y}} \quad (17)$$

where $(\mathbf{D})_i$ is the ith column of the matrix $\mathbf{D}$. The iterative updates according to (7) make $\mathbf{y}$ converge to an optimum. The convergence of the iterative computation is guaranteed by the Baum–Eagon inequality [44].

VI. IMPROVING ENDMEMBER EXTRACTION TECHNIQUES VIA DSS

When implementing an endmember extraction technique, we normally assume that the number of endmembers M in a hyperspectral image $\mathbf{X}$ should be known as prior information. Based on the information, M endmembers are identified by the endmember extraction technique. If an estimated number of endmembers $M_l < M$ is provided for the endmember extraction technique, at most M_l correct endmembers can be extracted and at least $M - M_l$ endmembers would be ignored. On the other hand, if the endmember extraction technique, e.g., vertex component analysis (VCA) [45], is informed of an estimated number of endmembers $M_g > M$ (in Section VII-A2, we use the DS method to improve the traditional VCA algorithm, and the value of M_g is 50), it extracts M_g candidate endmembers that include the M true endmembers. This observation makes sense for most endmember extraction techniques because they tend to extract a pixel, which is most different from others as an endmember from iteration to iteration such that the M endmember should be picked out before the iteration in which any of the $(M_g - M)$ nonendmembers are extracted. It is also observed that the $(M_g - M)$ extracted nonendmembers are not as discriminative as the M endmembers. The addition of the subset of the $(M_g - M)$ nonendmembers to the subset of M endmembers increases the likeness of the M endmembers and, in turn, reduces their divergent degree.

In the light of these observations, we use the DS as a postprocessing procedure for finely pruning the M_g candidate endmembers extracted by the original endmember extraction technique. Specifically, we consider the candidate endmembers as a set and perform endmember extraction by computing the DS of the candidate endmember set.

In this scenario, a novel improved endmember estimation strategy is established according to the following three steps. First, we assume the number of endmembers to be M_g, which is far greater than the actual number of endmembers M. Second, based on the assumption, we apply an endmember extraction technique, e.g., VCA, to a hyperspectral image to obtain a set of M_g of candidate endmembers. Third, we compute the DS of the candidate endmember set. The DS cardinality is the number of endmembers, and the hyperspectral pixels in DS are the endmembers.

One advantage of the strategy of the endmember extraction improvement based on DSs is that it shares the effectiveness of

an endmember extraction technique in determining individual endmembers and avoids its limitation on the prior knowledge of the number of endmembers. Therefore, the DS methodology provides a foundation stone for improving existing endmember extraction techniques.

VII. EXPERIMENTAL RESULTS

We use both synthetic data and real data to evaluate the performance of the proposed DS methodology in extracting and counting endmembers. The experimental results are compared with eight EEAs, i.e., ADVMM [34], SDVMM [34], AVMAX [35], SVMAX [35], p-norm-based pure pixel identification (TRIP) [27], ATGP [33], NABO [36], and SGA [32]. In addition, we experimentally compare the performance of the DS, Hysime [25], HFC analysis [26], and the AH (GENE-AH) algorithm [27] in estimating the number of endmembers.

We use three metrics, i.e., spectral information divergence (SID), abundance information divergence (AID), and root-mean-square error (RMSE) to evaluate the performance of endmember extraction of the DS method and the comparison algorithms. Let $\mathbf{X}_e = [\mathbf{x}_1, \mathbf{x}_2, \ldots, \mathbf{x}_m, \ldots, \mathbf{x}_M] \in \mathbb{R}^{L \times M}$ denote the true endmember signatures and $\hat{\mathbf{X}} = [\hat{\mathbf{x}}_1, \hat{\mathbf{x}}_2, \ldots, \hat{\mathbf{x}}_m, \ldots, \hat{\mathbf{x}}_M] \in \mathbb{R}^{L \times M}$ be the estimated endmember signatures, where M is the number of endmembers, $\mathbf{x}_m = [x_{1m}, x_{2m}, \ldots, x_{lm}, \ldots, x_{Lm}]^{\mathrm{T}} \in \mathbb{R}^{L \times 1}$, and $\hat{\mathbf{x}}_m = [\hat{x}_{1m}, \hat{x}_{2m}, \ldots, \hat{x}_{lm}, \ldots, \hat{x}_{Lm}]^{\mathrm{T}} \in \mathbb{R}^{L \times 1}$. The probability distribution vector of the mth true endmember signature is given by $\mathbf{p}_m = (\mathbf{x}_m / \sum_{l=1}^{L} x_{jm})$. The vector characterizes the variability of spectral signatures. Let $\mathbf{P}_e = [\mathbf{p}_1, \mathbf{p}_2, \ldots, \mathbf{p}_m, \ldots, \mathbf{p}_M] \in \mathbb{R}^{L \times M}$ be the probability distribution matrix for $\hat{\mathbf{X}}_e$, $\hat{\mathbf{P}} = [\hat{\mathbf{p}}_1, \hat{\mathbf{p}}_2, \ldots, \hat{\mathbf{p}}_m, \ldots, \hat{\mathbf{p}}_M] \in \mathbb{R}^{L \times M}$ represent the probability distribution matrix for $\hat{\mathbf{X}}_e$, p_{lm} be the (i, j)th element of matrix $\mathbf{P}_e$, and $\hat{p}_{lm}$ be the (i, j)th element of matrix $\hat{\mathbf{P}}$. We have the following equation:

$$D(\mathbf{x}_m | \hat{\mathbf{x}}_m) = \sum_{l=1}^{L} p_{lm} \log \frac{p_{lm}}{\hat{p}_{lm}}. \tag{18}$$

The relative entropy between $\mathbf{X}_e$ and $\hat{\mathbf{X}}$ is $D(\mathbf{X}_e | \hat{\mathbf{X}}) = [D(\mathbf{x}_1 | \hat{\mathbf{x}}_1), D(\mathbf{x}_2 | \hat{\mathbf{x}}_2), \ldots, D(\mathbf{x}_M | \hat{\mathbf{x}}_M)] \in \mathbb{R}^{1 \times M}$. The relative entropy is asymmetric with respect to $\mathbf{X}_e$ and $\hat{\mathbf{X}}$. To render a symmetric metric based on the relative entropy, the SID [46] is given by

$$\text{SID} = D(\mathbf{X}_e | \hat{\mathbf{X}}) + D(\hat{\mathbf{X}} | \mathbf{X}_e). \tag{19}$$

In order to make comparisons based on more comprehensive metrics, the abundance $\hat{\mathbf{a}}$ for one pixel $\mathbf{x}$ with respect to the estimated endmembers $\hat{\mathbf{X}}$ is employed, and each element of $\hat{\mathbf{a}} = [\hat{a}_1, \hat{a}_2, \ldots, \hat{a}_M]^{\mathrm{T}} \in \mathbb{R}^{M \times 1}$ represents the abundance with respect to one endmember. Let $\mathbf{q} \in \mathbb{R}^{L \times 1}$ denote additive noise, and the abundance in terms of a linear mixture method [47] is given as follows:

$$\mathbf{x} = \hat{\mathbf{X}}\hat{\mathbf{a}} + \mathbf{q} \tag{20}$$

subject to the nonnegative and sum-to-one constraints

$$\hat{a}_m \geq 0, \; m = 1, 2, \ldots, M; \; \sum_{m=1}^{M} \hat{a}_m = 1. \tag{21}$$

The abundance vectors are used to replace the endmember signatures in SID to derive more comprehensive metrics. Let $\mathbf{A}_e = [\mathbf{a}_1, \mathbf{a}_2, \ldots, \mathbf{a}_n, \ldots, \mathbf{a}_N] \in \mathbb{R}^{M \times N}$ denote the true endmember abundance and $\hat{\mathbf{A}} = [\hat{\mathbf{a}}_1, \hat{\mathbf{a}}_2, \ldots, \hat{\mathbf{a}}_n, \ldots, \hat{\mathbf{a}}_N] \in \mathbb{R}^{M \times N}$ be the estimated endmember abundance. Accordingly, the AID is given as follows:

$$\text{AID} = D(\mathbf{A}_e | \hat{\mathbf{A}}) + D(\hat{\mathbf{A}} | \mathbf{A}_e). \tag{22}$$

The matrix $\mathbf{R}$ is $(\mathbf{A}_e - \hat{\mathbf{A}})$, and R_{ij} is the (i, j)th element of the matrix $\mathbf{R}$. The RMSE is given as follows:

$$\text{RMSE} = \sqrt{\frac{\sum_{i=1}^{N} \sum_{j=1}^{M} R_{ij}^4}{NM}}. \tag{23}$$

The value of zero indicates the best endmember extraction performance in terms of the metrics SID, AID, or RMSE. Therefore, the value of the metric close to zero indicates accurate endmember extraction.

A. Experimental Evaluations on Synthetic Data

The synthetic data are created based on the United States Geological Survey (USGS) mineral spectra library.[2] We generate synthetic data partially based on the linear mixture method by Miao and Qi [48]. The linear mixture method provides two families of synthetic data: 1) synthetic data with no pure pixels and 2) synthetic data with multiple pure pixels for each type of material. In our experiments, we test our methods in three scenarios. In the first scenario, we incorporate one pure pixel for each material type into the synthetic data from family 1. We, thus, create our synthetic data with one pure pixel for each type of material. In the second scenario, we use the synthetic data from family 2 directly as our synthetic data with multiple pure pixels for each type of material. Fig. 1 shows the visualization results of the first and second scenarios. In the third scenario, we add zero-mean Gaussian noise to family 2 as our synthetic data to evaluate the robustness of the DS method to noise.

The original hyperspectral data do not guarantee to maintain a metric space in which the feature distance can be conveniently measured. In order to compute the feature distance in a principled manner, we commence by mapping the original hyperspectral data into a low-dimensional space via PCA. The Euclidean distance is used for measuring the feature distance between pixels in the low-dimensional space, resulting in the feature distance matrix $\mathbf{D}$. We compute the DS indicator $\mathbf{y}$ based on (17). The endmembers are extracted by identifying the nonzero elements in the DS indicator $\mathbf{y}$. Accordingly, the number of nonzero elements is the number of endmembers.

It is worth noting that we use PCA to automatically map the original hyperspectral data into a dimension reduction space to obtain dimension reduction data. We first compute the eigenvalues and eigenvectors of the covariance matrix of the original data. We then compute cumulative contribution rate of the eigenvalues and use the eigenvectors corresponding to the eigenvalues whose the cumulative contribution rate exceeds 99.99% as the projection matrix. We finally use the projection

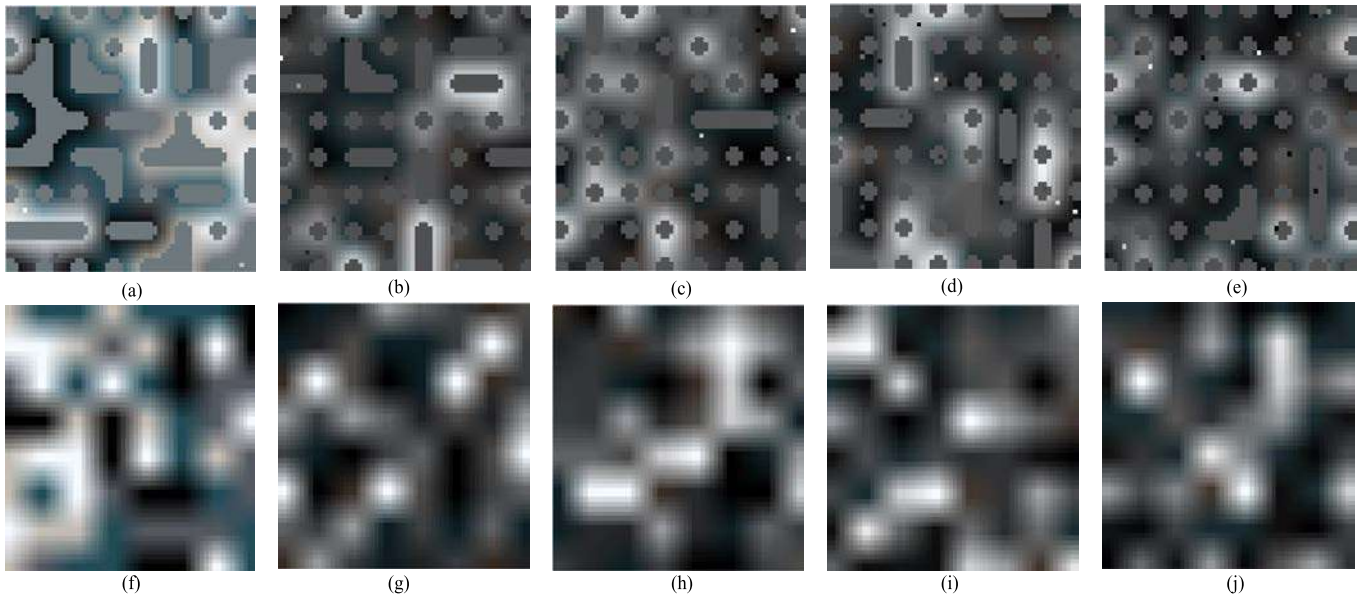[2]https://speclab.cr.usgs.gov/spectral-lib.html

Fig. 1.   Visualization results of synthetic data with different numbers of endmembers, i.e., 5, 10, 15, 20, and 25. (a)–(e) Synthetic data with one pure pixel for each type of material. (f)–(j) Synthetic data with multiple pure pixels for each type of material.
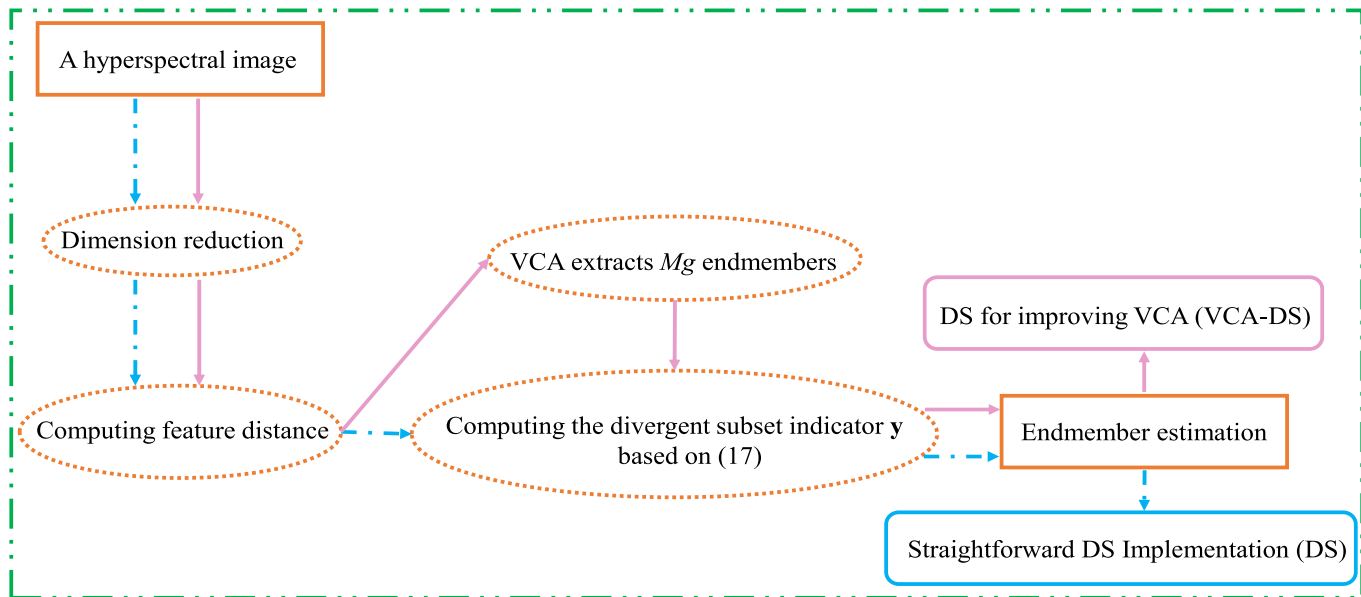

Fig. 2.   Flowchart of two different endmember estimation methods. Dashed dotted line: method of the straightforward DS implementation. Solid line: method of the DS for improving VCA (VCA-DS).

matrix to compute the dimension reduction data. It is also worth noting that more sophisticated data mapping techniques, such as manifold embedding methods, can be applied instead of PCA. Furthermore, more comprehensive distance functions, such as the Manhattan distance and the Mahalanobis distance, can be used rather than the straightforward Euclidean distance. Although the alternative strategies have potentials for improving the effectiveness of feature distance computation, we use the basic PCA and the Euclidean distance in this article because we aim to examine the effectiveness of our DS method even in the situation that the most elementary feature computation strategies are applied. Fig. 2 shows how to complete

the overall endmember estimation task by straightforward DS implementation and the DS for improving VCA.

1) Straightforward DS Implementation: We directly utilize DSs on synthetic data with one pure pixel and multiple pure pixels for each type of material. We obtain the divergent indicator **y** based on (17), and the nonzero elements in **y** are endmembers. Specially, the endmembers tend to be redundant, and multiple pure pixels might be identified for one type of material. To eliminate the redundancy, we compute the correlation matrix for the preliminary selection of endmembers. The standard correlation greater than a thresholding value (i.e., 0.99 in our experiments) indicates high correlation
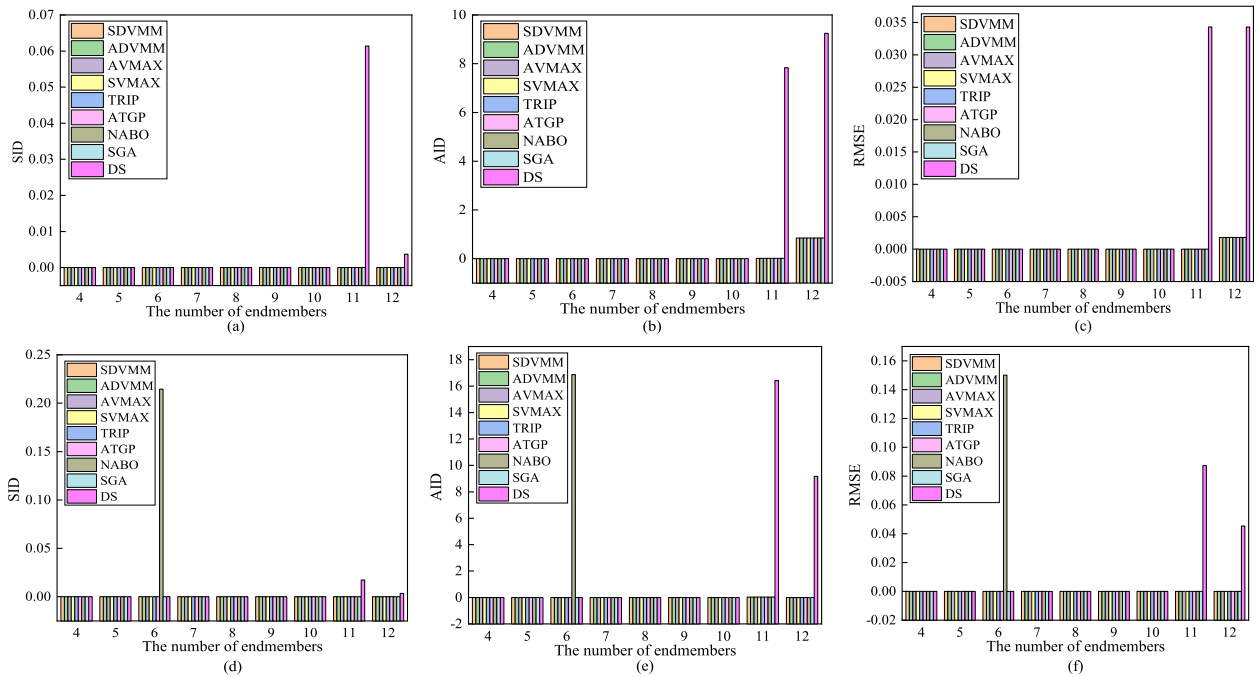
Fig. 3. Performance of the endmember extraction stage. (a)–(c) Synthetic data with one pure pixel for each type of material. (d)–(f) Synthetic data with multiple pure pixels for each type of material.
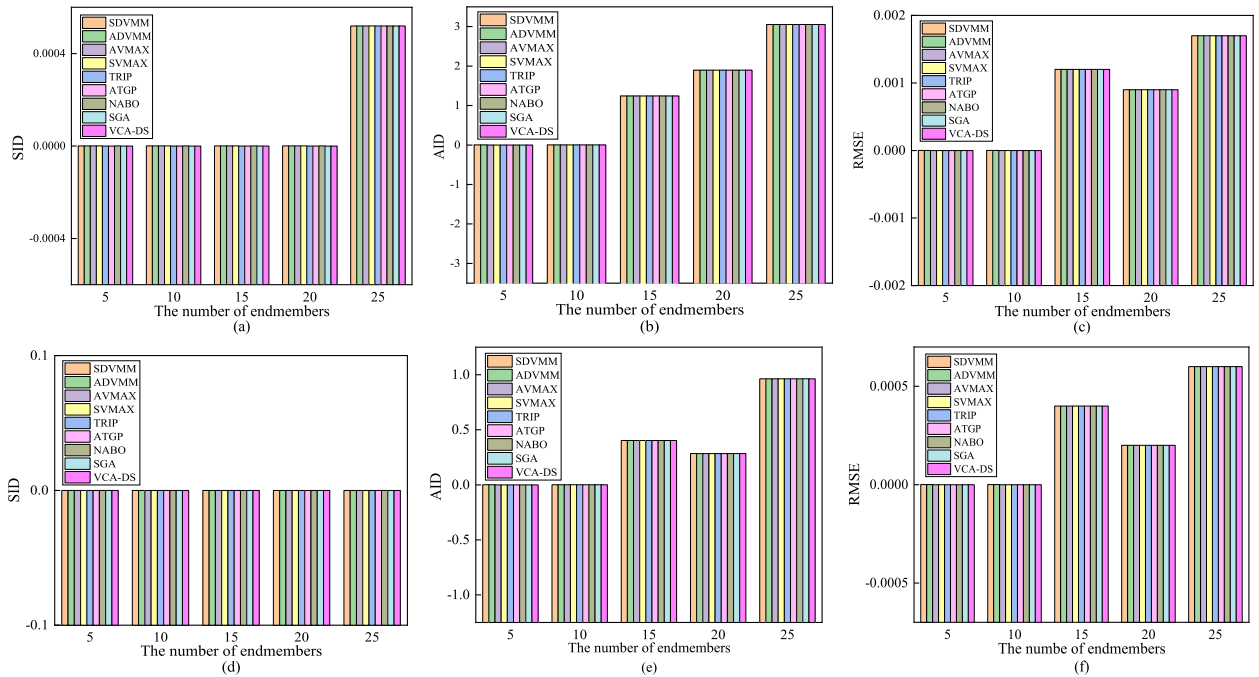

Fig. 4. Performance of extracting endmembers. (a)–(c) Synthetic data with one pure pixel for each type of material. (d)–(f) Synthetic data with multiple pure pixels for each type of material.

between pixels. Pixels that satisfy such high correlation condition in the preliminary selection are considered as multiple pure pixels for one type of material, and only one of them is used as an extracted endmember. We employ the metrics SID, AID, and RMSE to evaluate the endmember extraction performance. Each performance metric indicates an accurate result when its value is close to zero. Fig. 3 illustrates the

accuracy of different methods in extracting endmembers on different synthetic data. The values of the metrics SID, AID, and RMSE are almost close to zero for eight comparison methods, and the NABO method has an error when the number of endmembers is six on synthetic data with multiple pure pixels for each type of material. Though the performance of the straightforward DS implementation keeps accurate for
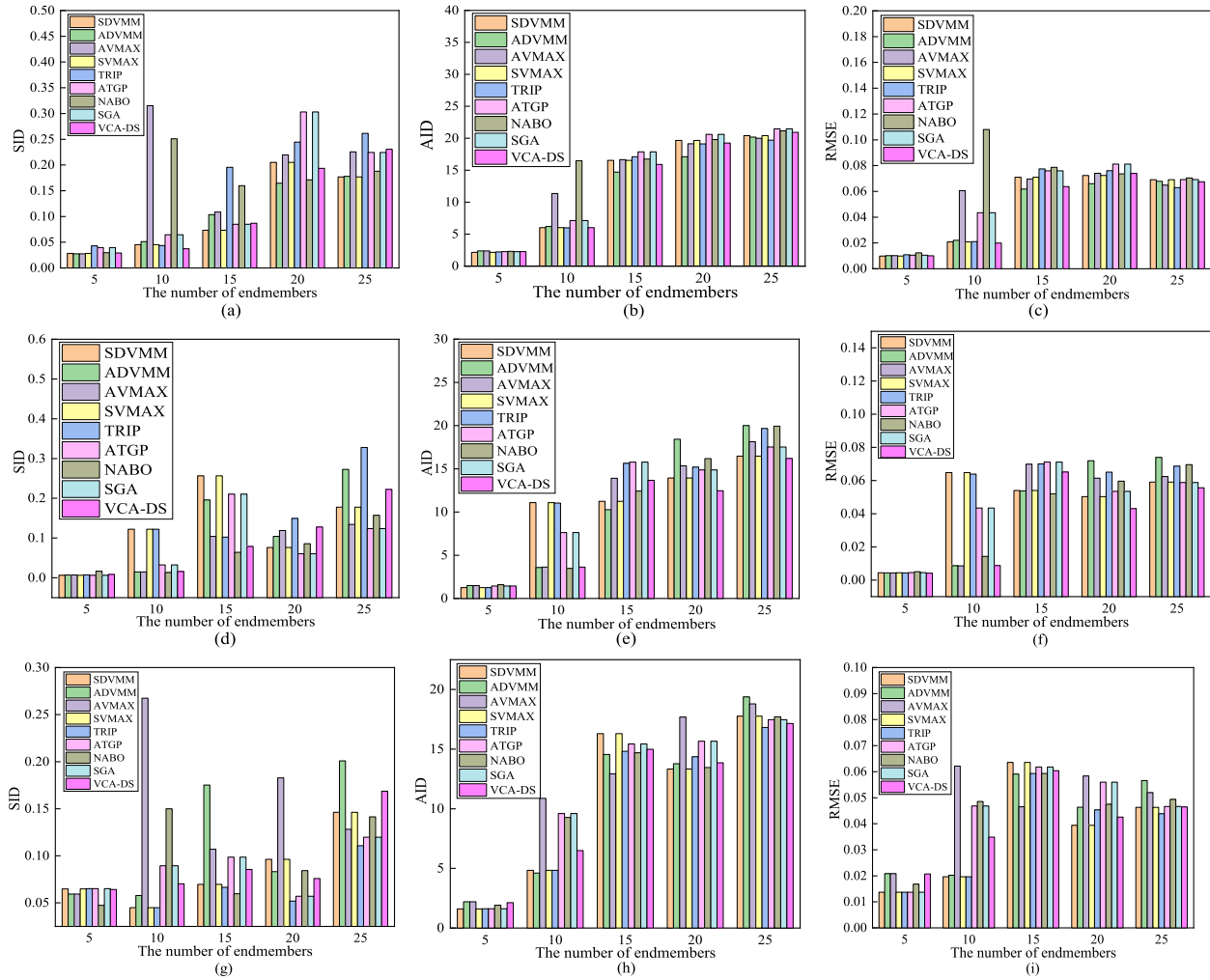
Fig. 5. Performance of extracting endmembers on synthetic data with different noises. (a)–(c) SNR = 10 dB. (d)–(f) SNR = 15 dB. (g)–(i) SNR = 20 dB.

counting a medium number of endmembers, it decreases when the number of endmembers exceeds ten. One possible reason for this inefficiency is that the pairwise relationships encoded by the DS are low order descriptions that are easily contaminated by noisy and interfering observations. To cope with this inefficiency of DSs for counting large numbers of endmembers, we extend our straightforward strategy to that described in Section VII-A2 and present the experimental evaluation in the following sections.

2) DSs for Improving VCA: To neutralize the susceptibility of DSs to noisy and interfering observations, we have proposed an improvement strategy in Section VI. Specifically, we commence by performing VCA on the original data with an assumed number of endmembers 50, which is evidently greater than the actual number of endmembers, and obtain a preliminary endmember extraction result. We then perform DSs on the preliminary result and obtain the divergent indicator **y**, and the nonzero elements in the **y** are endmembers. We refer to the novel strategy as VCA-DS. Fig. 4 shows the results of different methods. We observe that our VCA-DS method is an effective method for endmember extraction, and it is not limited by the large number of endmembers. The reason for SID, AID,

and RMSE exhibiting very small values in Figs. 3 and 4 is that the two types of synthetic data contain no noise, and the endmember spectrums extracted by DS and VCA-DS are the same as the reference spectrums.

Fig. 5 compares the performance of extracting endmembers for different methods at various noise levels. The metrics SID, AID, and RMSE are used to evaluate the sensitivity of different methods in extracting endmembers to various noise (10, 15, and 20 dB). We observe that the VCA-DS method is stable compared to other methods in extracting endmembers when the noise is different.

Fig. 6 shows a qualitative comparison between the endmembers extracted via the VCA-DS method and their corresponding true spectral signatures from the USGS spectra library. From Fig. 6, we observe that the endmember signatures estimated by the VCA-DS method are in good agreement with the reference USGS spectral signatures. The results shown in Fig. 6 reflect that the high accuracy of VCA-DS in endmember extraction. All experimental evaluations about endmember extraction validate that the VCA-DS method is effective in endmember extraction without the prior knowledge of the number of endmembers.
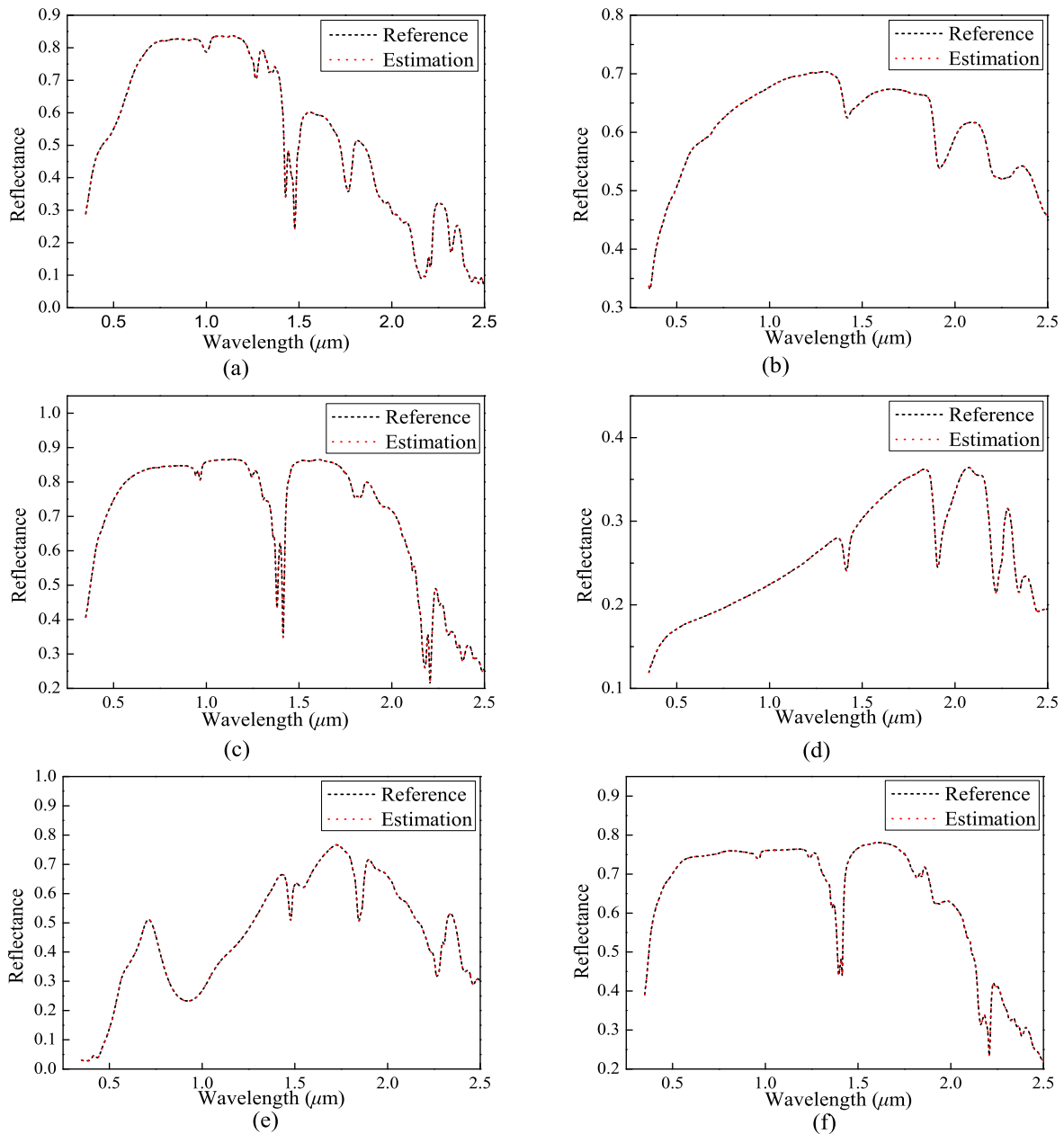
Fig. 6.   Reference signatures and estimated endmember signatures by VCA-DS method on synthetic data. (a) Alunite. (b) Chalcedony. (c) Dickite. (d) Illite. (e) Jarosite. (f) Kaolinite.

Fig. 7 reports the performance of the VCA-DS method in counting endmembers on synthetic data with one pure pixel and multiple pure pixels for each type of material. As shown in Fig. 7, the Hysime method has errors when the number of endmembers exceeds 15 and 20 on the synthetic data with one pure pixel and multiple pure pixels for each type of material, respectively. Fig. 7 also reveals that the VCA-DS method and the two traditional methods (HFC and GENE-AH) achieve accurate estimations about the number of endmembers.

Tables I and II show the running average time of different methods in extracting and counting endmembers on different types of synthetic data. NABO and HFC are the fastest methods in extracting and counting endmembers, respectively. The difference in the average running time of different methods is very small. Especially, the VCA-DS method completes the overall endmember estimation task, i.e., extracting and counting endmembers, and other methods only complete one task, i.e., either endmember counting or endmember extraction. Therefore, VCA-DS is an efficient method in both extracting and counting endmembers.

3) Observations: We have empirically evaluated our DS methodology in two different tasks, i.e., endmember extraction and endmember counting. Each comparison method is only suited to one of the two tasks, and in contrast, our DS method simultaneously conducts both tasks. In addition, our DS method achieves comparable results in both tasks with the task-specific state of the art methods.

The derivative of the DS method, i.e., the VCA-DS method, can be viewed from two perspectives. On one hand, VCA can be viewed as a preprocessing step for DSs. It primarily filters
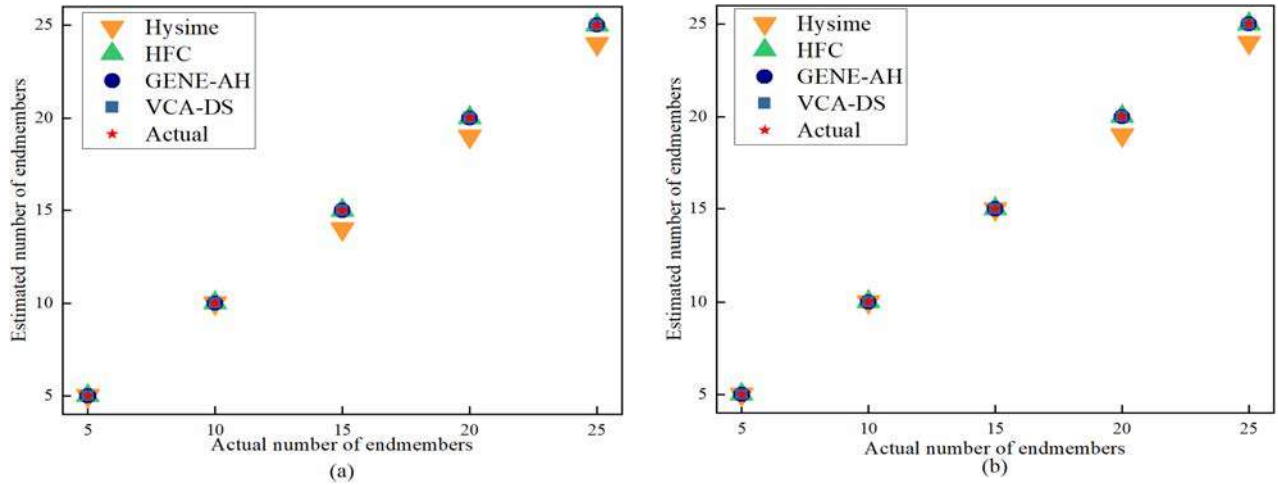
Fig. 7. Performance of counting endmembers. (a) Synthetic data with one pure pixel for each type of material. (b) Synthetic data with multiple pure pixels for each type of material.

TABLE I
AVERAGE RUNNING TIME (SECOND) FOR EXTRACTING ENDMEMBERS ON SYNTHETIC DATA

Data type	Methods								
	SDVMM	ADVMM	AVMAX	SVMAX	TRIP	ATGP	NABO	SGA	VCA-DS
One pure pixel	1.4794	1.4703	1.5394	1.4797	1.4235	1.1476	**1.1003**	1.3824	1.5087
Multiple pure pixels	1.2249	1.2035	1.2120	1.1393	1.0821	0.9724	**0.8612**	1.1366	1.1553
Multiple pure pixels (10db noise)	1.5179	1.5384	1.4853	1.4039	1.4253	1.2495	**1.1283**	1.4616	2.3318
Multiple pure pixels (15db noise)	1.5120	1.5747	1.4695	1.4348	1.4236	1.3104	**1.1463**	1.4792	2.3011
Multiple pure pixels (20db noise)	1.6468	1.7343	1.6237	1.5999	1.5910	1.3606	**1.2940**	1.6055	2.5154

TABLE II
AVERAGE RUNNING TIME (SECOND) FOR COUNTING
ENDMEMBERS ON SYNTHETIC DATA

Data type	Methods			
	Hysime	HFC	GENE-AH	VCA-DS
One pure pixel	0.1456	**0.0806**	5.4391	1.5087
Multiple pure pixels	0.1636	**0.0775**	5.5262	1.1553

out the noisy and interweaving pixels that are definitely not endmembers but just interferes with endmember estimation and leaves comparatively clean pixels from which endmembers are simultaneously counted and extracted via the DS method. On the other hand, as described in Section VII-A2, the DS method can be considered as a postprocessing procedure that improves the effectiveness of VCA without the prior knowledge of the number of endmembers. Therefore, VCA and the DS method are complementary to each other, and the

VCA-DS strategy forms an effective framework for simultaneously counting and extracting endmember. It is robust and scalable to large numbers of endmembers.

B. Experimental Evaluations on Real Data

1) GOCI Data: We empirically test the DS method on GOCI data that covers an ocean region with the existence of green algae. Specifically, we test the DS method in terms of computing the abundance with respect to its extracted green algae endmember and accordingly estimating the green algae area.

The GOCI data have eight bands and 1219×1175 pixels. We use the DS method to extract endmembers from the GOCI image. In our experiments, the DS method automatically extracts two endmembers, each of which is denoted by $\hat{\mathbf{x}}_\beta = [x_1, x_2, \ldots, x_L]^{\mathrm{T}}$. In order to determine which endmember represents the green algae, we use the green algae spectrum provided by the China State Oceanic Administration (CSOA) as the reference spectrum $\mathbf{r} = [r_1, r_2, \ldots, r_L]^{\mathrm{T}}$ to identify the green algae endmember. Specifically, we compute the spectral angle $\arccos(\mathbf{r}^{\mathrm{T}}\hat{\mathbf{x}}_\beta / |\mathbf{r}|^{-1/2}|\hat{\mathbf{x}}_\beta|^{-1/2})$ between the spectrum of each extracted endmember and the reference spectrum.
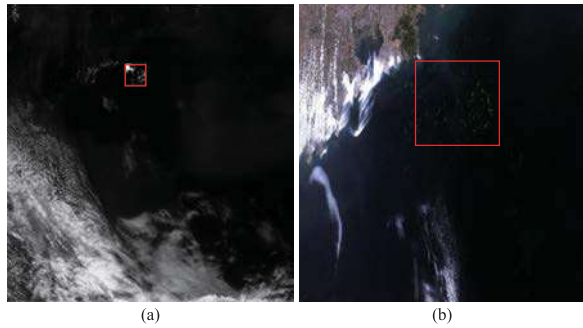
Fig. 8. Investigated ocean region with existence of green algae. (a) GOCI image. (b) HJ-1B image. The GOCI image and HJ-1B image collected on June 29, 2013. The same investigated regions are cropped from both the GOCI image and the HJ-1B images with the red rectangles, separately. The sizes of the cropped patches look different because of the different resolutions of the GOCI image and HJ-1B image.

We consider the endmember with the smallest angle to be the green algae endmember.

We compute the abundance based on (20). We estimate the area B of green algae blooms as follows:

$$B = S^2 \sum_{i=1}^{N} \hat{a}(i) \tag{24}$$

where $\hat{a}(i)$ denotes the green algae abundance of the ith pixel in the GOCI image, and S is the spatial resolution of GOCI image. The spatial resolution of the GOCI image used in our experiments is $R = 500$m. The green algae area is 69.18 km^2. To evaluate the accuracy of the green algae area estimation, we use the HJ-1B data that were collected at a close time to that of the GOCI data as the reference data. We consider that the GOCI and HJ-1B images capture the same scene at the same time. We manually segment the investigated ocean regions from the GOCI image and HJ-1B image by rectangles, as shown in Fig. 8(a) and (b), respectively. Though surrounding the same region, the two rectangles appear in different sizes in Fig. 8 because of the different resolutions of the GOCI image and HJ-1B image.

We used the green algae area 83.75 km^2, which is computed based on the HJ-1B data as the baseline. The area estimated via the DS method is close to the baseline. The results of the green algae area on GOCI and HJ-1B data reflect that the DS method extracts and counts endmembers effectively.

It is worth noting that the green algae area estimated by the DS method and the cofactor N-FINDR method [29] are different. The original assumption of the number of endmembers for the GOCI data with no cropping is four [30], and the cofactor N-FINDR method uses the assumption without considering that the image cropping would reduce the number of endmembers. Benefiting from the effectiveness of the DS method with more accurate endmember estimation, the green algae area estimated by the DS method is more accurate than that by the cofactor N-FINDR method reported in [29].

2) Samson, Jasper Ridge, Urban, and Cuprite Data: We utilize four real data[3] to evaluate the performance of the VCA-DS method in counting endmembers.

TABLE III
RESULTS OF ESTIMATED NUMBER OF ENDMEMBERS BY
DIFFERENT METHODS ON FOUR REAL DATA

Methods	Real data			
	Samson	Jasper Ridge	Urban	Cuprite
Hysime	43	18	27	13
HFC	5	3	**6**	**12**
GENE-AH	4	**4**	4	18
DS	**3**	**4**	7	**12**
Actual number	3	4	6	12

The first real data is Samson, which contains three endmembers. Samson has 952×952 pixels, each of which has 156 bands covering the wavelengths from 401 to 889 nm. The original image is too large, leading to very expensive in terms of computational cost. In this article, a region of 95×95 pixels is used. The second real data are Jasper Ridge, which has four endmembers. The Jasper Ridge data have 210 bands and 512×614 pixels with wavelengths ranging from 380 to 2500 nm. We crop the original image into a subimage of 100×100 pixels. The position of the first pixel is (105, 269). We remove the bands 1–3, 108–112, 154–166, and 220–224 (due to dense water vapor and atmospheric effects) and keep 198 bands in our experiments. The third real data is Urban that has four endmembers. The Urban data have 307×307 pixels with wavelengths ranging from 400 to 2500 nm. We remove the bands 1–4, 76, 87, 101–111, 136–153, and 198–210 (due to dense water vapor and atmospheric effects), and the modified data have 162 bands. The forth real data are the Cuprite [49]–[51], and it has 12 endmembers and covers the Cuprite in Las Vegas, USA. Cuprite has 224 bands with 250×190 pixels, and the wavelength ranges from 370 to 2480 nm. We remove some noisy bands (1–2 and 221–224) and water absorption bands (104, 113, 148, and 167) from the original 224 bands, and the modified Cuprite data have 188 bands. The abovementioned four real data are shown in Fig. 9.

Table III shows the performance of different algorithms in counting endmembers. According to our experiments, Hysime could not obtain accurate results on any real data set. HFC achieves accurate performance on Urban and Cuprite data. GENE-AH obtains accurate results on the Jasper Ridge data, and the DS method produces accurate results on Samson, Jasper Ridge, and Cuprite data and just has a minor error on the Urban data.

Our VCA-DS method simultaneously counts and extracts endmembers in the real data. Our experiments validate that it extracts accurate endmembers for the real data. Due to the page limitation, we did not illustrate the endmember extraction results here. Interested readers can conduct experiments following our settings. Our full code is released for public evaluation.[4]

[3]http://lesun.weebly.com/hyperspectral-dataset.html
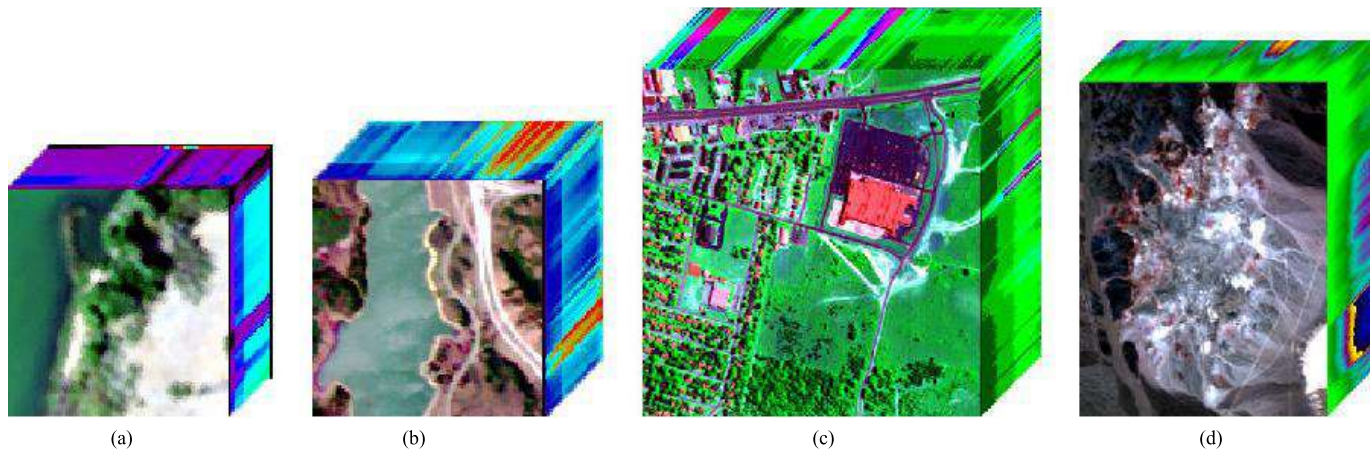
[4]https://github.com/xuanwentao/DivergentSubset

Fig. 9.   Four different real data. (a) Samson. (b) Jasper Ridge. (c) Urban. (d) Cuprite.

VIII. CONCLUSION AND FUTURE WORK

We have developed a new endmember estimation methodology, referred to DSs, for simultaneously counting and extracting in a hyperspectral image. The DS has been validated to be capable of counting and extracting a medium number of endmembers. However, due to the limited capability of pairwise characterization in the DS method, it does not scale up to a large number of endmembers in the condition of noisy and interfering observations. To address this limitation, we have developed a new DS-based strategy that first uses an existing endmember extraction technique (e.g., VCA) to extract an arbitrarily large number of candidate endmembers and then uses the DS method to count and extract the actual endmembers in the candidates. This strategy has been validated to be effective to be scaled up to a large number of endmembers, without the requirement of the number of endmembers.

As with any new approach, there are some unresolved issues that may present challenges over time. Specifically, the DS method is one of the first available methods able to simultaneously extract endmember signatures and estimate their number in a hyperspectral scene. One limitation of the DS method is the assumption of the existence of pure pixels in the hyperspectral image. In our future work, we will investigate how to simultaneously determine the number of endmembers and extract the endmember signatures from hyperspectral images without pure pixels.

REFERENCES

[1] G. Wang, G. Dong, H. Li, L. Han, X. Tao, and P. Ren, "Remote sensing image synthesis via graphical generative adversarial networks," in *Proc. IEEE Int. Geosci. Remote Sens. Symp. (IGARSS)*, Jul. 2019, pp. 10027–10030.

[2] M. E. Paoletti, J. M. Haut, X. Tao, J. P. Miguel, and A. Plaza, "A new GPU implementation of support vector machines for fast hyperspectral image classification," *Remote Sens.*, vol. 12, no. 8, p. 1257, 2020.

[3] F. Luo, B. Du, L. Zhang, L. Zhang, and D. Tao, "Feature learning using spatial-spectral hypergraph discriminant analysis for hyperspectral image," *IEEE Trans. Cybern.*, vol. 49, no. 7, pp. 2406–2419, Jul. 2019.

[4] N. He *et al.*, "Feature extraction with multiscale covariance maps for hyperspectral image classification," *IEEE Trans. Geosci. Remote Sens.*, vol. 57, no. 2, pp. 755–769, Feb. 2019.

[5] F. Gao, Y. Zhang, J. Wang, J. Sun, E. Yang, and A. Hussain, "Visual attention model based vehicle target detection in synthetic aperture radar images: A novel approach," *Cognit. Comput.*, vol. 7, no. 4, pp. 434–444, Aug. 2015.

[6] F. Gao *et al.*, "Biologically inspired progressive enhancement target detection from heavy cluttered SAR images," *Cognit. Comput.*, vol. 8, no. 5, pp. 955–966, Oct. 2016.

[7] F. Gao, F. Ma, J. Wang, J. Sun, E. Yang, and H. Zhou, "Visual saliency modeling for river detection in high-resolution SAR imagery," *IEEE Access*, vol. 6, no. 1, pp. 1000–1014, 2018.

[8] A. Erturk, M.-D. Iordache, and A. Plaza, "Sparse unmixing-based change detection for multitemporal hyperspectral images," *IEEE J. Sel. Topics Appl. Earth Observ. Remote Sens.*, vol. 9, no. 2, pp. 708–719, Feb. 2016.

[9] A. Erturk, M.-D. Iordache, and A. Plaza, "Sparse unmixing with dictionary pruning for hyperspectral change detection," *IEEE J. Sel. Topics Appl. Earth Observ. Remote Sens.*, vol. 10, no. 1, pp. 321–330, Jan. 2017.

[10] B. Du, L. Ru, C. Wu, and L. Zhang, "Unsupervised deep slow feature analysis for change detection in multi-temporal remote sensing images," *IEEE Trans. Geosci. Remote Sens.*, vol. 57, no. 12, pp. 9976–9992, Dec. 2019.

[11] R. Wang, H.-C. Li, A. Pizurica, J. Li, A. Plaza, and W. J. Emery, "Hyperspectral unmixing using double reweighted sparse regression and total variation," *IEEE Geosci. Remote Sens. Lett.*, vol. 14, no. 7, pp. 1146–1150, Jul. 2017.

[12] R. Fernandez-Beltran, A. Plaza, J. Plaza, and F. Pla, "Hyperspectral unmixing based on dual-depth sparse probabilistic latent semantic analysis," *IEEE Trans. Geosci. Remote Sens.*, vol. 56, no. 11, pp. 6344–6360, Nov. 2018.

[13] J. Delgado, G. Martin, J. Plaza, L. I. Jimenez, and A. Plaza, "Fast spatial preprocessing for spectral unmixing of hyperspectral data on graphics processing units," *IEEE J. Sel. Topics Appl. Earth Observ. Remote Sens.*, vol. 9, no. 2, pp. 952–961, Feb. 2016.

[14] F. Kowkabi, H. Ghassemian, and A. Keshavarz, "A fast spatial-spectral preprocessing module for hyperspectral endmember extraction," *IEEE Geosci. Remote Sens. Lett.*, vol. 13, no. 6, pp. 782–786, Jun. 2016.

[15] L. Drumetz *et al.*, "Hyperspectral local intrinsic dimensionality," *IEEE Trans. Geosci. Remote Sens.*, vol. 54, no. 7, pp. 4063–4078, Jul. 2016.

[16] R. Heylen, M. Parente, and P. Scheunders, "Estimation of the number of endmembers via the hubness phenomenon," in *Proc. 8th Workshop Hyperspectral Image Signal Process., Evol. Remote Sens. (WHISPERS)*, Aug. 2016, pp. 1–4.

[17] Z. Li, J. Li, and G. Wang, "Estimating the number of endmembers from hyperspectral image using noncentral chi-squared distribution model," in *Proc. IEEE Int. Geosci. Remote Sens. Symp. (IGARSS)*, Jul. 2016, pp. 6577–6580.

[18] J. Rissanen, "Modeling by shortest data description," *Automatica*, vol. 14, no. 5, pp. 465–471, Sep. 1978.

[19] H. Akaike, "A new look at the statistical model identification," *IEEE Trans. Autom. Control*, vol. AC-19, no. 6, pp. 716–723, Dec. 1974.

[20] M. W. Graham and D. J. Miller, "Unsupervised learning of parsimonious mixtures on large spaces with integrated feature and component selection," *IEEE Trans. Signal Process.*, vol. 54, no. 4, pp. 1289–1303, Apr. 2006.

[21] A. Halimi, P. Honeine, M. Kharouf, C. Richard, and J.-Y. Tourneret, "Estimating the intrinsic dimension of hyperspectral images using a noise-whitened eigengap approach," *IEEE Trans. Geosci. Remote Sens.*, vol. 54, no. 7, pp. 3811–3821, Jul. 2016.

[22] E. Terreaux, J.-P. Ovarlez, and F. Pascal, "New model order selection in large dimension regime for complex elliptically symmetric noise," in *Proc. 25th Eur. Signal Process. Conf. (EUSIPCO)*, Aug. 2017, pp. 1090–1094.

[23] S. Das, A. Routray, and A. K. Deb, "Noise robust estimation of number of endmembers in a hyperspectral image by eigenvalue based gap index," in *Proc. 8th Workshop Hyperspectral Image Signal Processing: Evol. Remote Sens. (WHISPERS)*, Aug. 2016, pp. 1–5.

[24] P. R. Peres-Neto, D. A. Jackson, and K. M. Somers, "How many principal components? Stopping rules for determining the number of non-trivial axes revisited," *Comput. Statist. Data Anal.*, vol. 49, no. 4, pp. 974–997, Jun. 2005.

[25] J. M. Bioucas-Dias and J. M. P. Nascimento, "Hyperspectral subspace identification," *IEEE Trans. Geosci. Remote Sens.*, vol. 46, no. 8, pp. 2435–2445, Aug. 2008.

[26] C.-I. Chang and Q. Du, "Estimation of number of spectrally distinct signal sources in hyperspectral imagery," *IEEE Trans. Geosci. Remote Sens.*, vol. 42, no. 3, pp. 608–619, Mar. 2004.

[27] A. Ambikapathi, T.-H. Chan, C.-Y. Chi, and K. Keizer, "Hyperspectral data geometry-based estimation of number of endmembers using p-norm-based pure pixel identification algorithm," *IEEE Trans. Geosci. Remote Sens.*, vol. 51, no. 5, pp. 2753–2769, May 2013.

[28] N. Dobigeon, S. Moussaoui, M. Coulon, J.-Y. Tourneret, and A. O. Hero, "Joint Bayesian endmember extraction and linear unmixing for hyperspectral imagery," *IEEE Trans. Signal Process.*, vol. 57, no. 11, pp. 4355–4368, Nov. 2009.

[29] X. Tao, T. Cui, and P. Ren, "Cofactor-based efficient endmember extraction for green algae area estimation," *IEEE Geosci. Remote Sens. Lett.*, vol. 16, no. 6, pp. 849–853, Jun. 2019.

[30] B. Pan, Z. Shi, Z. An, Z. Jiang, and Y. Ma, "A novel spectral-unmixing-based green algae area estimation method for GOCI data," *IEEE J. Sel. Topics Appl. Earth Observ. Remote Sens.*, vol. 10, no. 2, pp. 437–449, Feb. 2017.

[31] X. Tao, T. Cui, Z. Yu, and P. Ren, "Locality preserving endmember extraction for estimating green algae area," in *Proc. OCEANS-MTS/IEEE Kobe Techno-Oceans (OTO)*, May 2018, pp. 1–4.

[32] C.-I. Chang, C.-C. Wu, C.-S. Lo, and M.-L. Chang, "Real-time simplex growing algorithms for hyperspectral endmember extraction," *IEEE Trans. Geosci. Remote Sens.*, vol. 48, no. 4, pp. 1834–1850, Apr. 2010.

[33] H. Ren and C.-I. Chang, "Automatic spectral target recognition in hyperspectral imagery," *IEEE Trans. Aerosp. Electron. Syst.*, vol. 39, no. 4, pp. 1232–1249, Oct. 2003.

[34] T.-H. Chan, J.-Y. Liou, A. Ambikapathi, W.-K. Ma, and C.-Y. Chi, "Fast algorithms for robust hyperspectral endmember extraction based on worst-case simplex volume maximization," in *Proc. IEEE Int. Conf. Acoust., Speech Signal Process. (ICASSP)*, Mar. 2012, pp. 1237–1240.

[35] T.-H. Chan, W.-K. Ma, A. Ambikapathi, and C.-Y. Chi, "A simplex volume maximization framework for hyperspectral endmember extraction," *IEEE Trans. Geosci. Remote Sens.*, vol. 49, no. 11, pp. 4177–4193, Nov. 2011.

[36] R. Marrero *et al.*, "A novel negative abundance-oriented hyperspectral unmixing algorithm," *IEEE Trans. Geosci. Remote Sens.*, vol. 53, no. 7, pp. 3772–3790, Jul. 2015.

[37] A. Marinoni, A. Plaza, and P. Gamba, "A novel preunmixing framework for efficient detection of linear mixtures in hyperspectral images," *IEEE Trans. Geosci. Remote Sens.*, vol. 55, no. 8, pp. 4325–4333, Aug. 2017.

[38] B. Du, Q. Wei, and R. Liu, "An improved quantum-behaved particle swarm optimization for endmember extraction," *IEEE Trans. Geosci. Remote Sens.*, vol. 57, no. 8, pp. 6003–6017, Aug. 2019.

[39] L. Tong, B. Du, R. Liu, and L. Zhang, "An improved multiobjective discrete particle swarm optimization for hyperspectral endmember extraction," *IEEE Trans. Geosci. Remote Sens.*, vol. 57, no. 10, pp. 7872–7882, Oct. 2019.

[40] M. Pavan and M. Pelillo, "Dominant sets and pairwise clustering," *IEEE Trans. Pattern Anal. Mach. Intell.*, vol. 29, no. 1, pp. 167–172, Jan. 2007.

[41] M. Pavan, "A new graph-theoretic approach to clustering, with applications to computer vision," Ph.D. dissertation, Univ. Ca' Foscari, Venice, Italy, 2004.

[42] M. Pavan and M. Pelillo, "A new graph-theoretic approach to clustering and segmentation," in *Proc. IEEE Comput. Soc. Conf. Comput. Vis. Pattern Recognit.*, Jun. 2003, p. 1

[43] J. W. Weibull, *Evolutionary Game Theory*, vol. 78, no. 3. Cambridge, MA, USA: MIT Press, 1996, pp. 850–853.

[44] L. E. Baum and J. A. Eagon, "An inequality with applications to statistical estimation for probabilistic functions of Markov processes and to a model for ecology," *Bull. Amer. Math. Soc.*, vol. 73, no. 3, pp. 360–364, May 1967.

[45] J. C. Harsanyi and C.-I. Chang, "Hyperspectral image classification and dimensionality reduction: An orthogonal subspace projection approach," *IEEE Trans. Geosci. Remote Sens.*, vol. 32, no. 4, pp. 779–785, Jul. 1994.

[46] C.-I. Chang and D. C. Heinz, "Constrained subpixel target detection for remotely sensed imagery," *IEEE Trans. Geosci. Remote Sens.*, vol. 38, no. 3, pp. 1144–1159, May 2000.

[47] J. Li, J. M. Bioucas-Dias, A. Plaza, and L. Liu, "Robust collaborative nonnegative matrix factorization for hyperspectral unmixing," *IEEE Trans. Geosci. Remote Sens.*, vol. 54, no. 10, pp. 6076–6090, Oct. 2016.

[48] L. Miao and H. Qi, "Endmember extraction from highly mixed data using minimum volume constrained nonnegative matrix factorization," *IEEE Trans. Geosci. Remote Sens.*, vol. 45, no. 3, pp. 765–777, Mar. 2007.

[49] F. Zhu, Y. Wang, S. Xiang, B. Fan, and C. Pan, "Structured sparse method for hyperspectral unmixing," *ISPRS J. Photogramm. Remote Sens.*, vol. 88, pp. 101–118, Feb. 2014.

[50] F. Zhu, Y. Wang, B. Fan, G. Meng, and C. Pan, "Effective spectral unmixing via robust representation and learning-based sparsity," 2014, *arXiv:1409.0685*. [Online]. Available: https://arxiv.org/abs/1409.0685

[51] F. Zhu, Y. Wang, B. Fan, G. Meng, S. Xiang, and C. Pan, "Spectral unmixing via data-guided sparsity," 2014, *arXiv:1403.3155*. [Online]. Available: https://arxiv.org/abs/1403.3155

Xuanwen Tao (Student Member, IEEE) received the B.S. degree in electronic information science and technology from Tianjin Chengjian University, Tianjin, China, in 2016. She is currently pursuing the M.Eng. degree in information and communication engineering with the China University of Petroleum (East China), Qingdao, China.

Her research interests include machine learning and hyperspectral data processing.

Tingwei Cui received the B.Eng., M.Eng., and Ph.D. degrees from the Ocean University of China, Qingdao, China, in 2000, 2003, and 2006, respectively.

He is currently a Professor with Sun Yat-sen University, China. Prior to that, he was a Professor with the First Institute of Oceanography, Ministry of Natural Resources of China, Beijing, China. His research interests are ocean optics and ocean color remote sensing.

Antonio Plaza (Fellow, IEEE) received the M.Sc. and Ph.D. degrees in computer engineering from the Hyperspectral Computing Laboratory, Department of Technology of Computers and Communications, University of Extremadura, Cáceres, Spain, in 1999 and 2002, respectively.

He is currently the Head of the Hyperspectral Computing Laboratory, Department of Technology of Computers and Communications, University of Extremadura. He is currently one of the top cited authors in Spain and in the University of Extremadura. He has guest edited ten special issues on hyperspectral remote sensing for different journals. His research interests include remotely sensed hyperspectral image analysis, signal processing, and efficient implementations of large-scale scientific problems on high-performance computing architectures, including commodity Beowulf clusters, heterogeneous networks of computers and clouds, and specialized computer architectures, such as field programmable gate arrays or graphical processing units.

Dr. Plaza is a fellow of the IEEE for the contributions to hyperspectral data processing and parallel computing of earth observation data. He was a recipient of a recognition as an Outstanding Associate Editor of IEEE ACCESS in 2017. He was a member of the Editorial Board of the IEEE GEOSCIENCE AND REMOTE SENSING NEWSLETTER from 2011 to 2012 and the *IEEE Geoscience and Remote Sensing Magazine* in 2013. He was also a pixel of the Steering Committee of the IEEE JOURNAL OF SELECTED TOPICS IN APPLIED EARTH OBSERVATIONS AND REMOTE SENSING. He is a reviewer of 500 manuscripts for over 50 different journals. He served as the Editor-in-Chief for the IEEE TRANSACTIONS ON GEOSCIENCE AND REMOTE SENSING from 2013 to 2017. He is an Associate Editor of IEEE ACCESS. He served as the Director of Education Activities for the IEEE Geoscience and Remote Sensing Society (GRSS) from 2011 to 2012 and the President of the Spanish Chapter of the IEEE GRSS from 2012 to 2016.

Peng Ren (Senior Member, IEEE) received the B.Eng. and M.Eng. degrees in electronic engineering from the Harbin Institute of Technology, Harbin, China, and the Ph.D. degree in computer science from the University of York, York, U.K.

He is currently a Professor with the College of Oceanography and Space Informatics, China University of Petroleum (East China), Qingdao, China. His research interests include remote sensing and machine learning.

Dr. Ren was a recipient of the K. M. Scott Prize from the University of York in 2011 and the Eduardo Caianiello Best Student Paper Award at the 18th International Conference on Image Analysis and Processing in 2015, as one coauthor.